# Elastic scattering of 60-MeV alpha particles by the even nickel isotopes*

D. G. Madland, P. Schwandt, and W. T. Sloan
*Physics Department, Indiana University, Bloomington, Indiana 47401*

P. Shapiro
*Naval Research Laboratory, Washington, D. C. 20375*

P. P. Singh
*Physics Department, Indiana University, Bloomington, Indiana 47401, and Naval Research Laboratory, Washington, D. C. 20375*

(Received 17 September 1973)

An optical-model analysis of the scattering of 60-MeV $\alpha$ particles by $^{58}$Ni, $^{60}$Ni, $^{62}$Ni, and $^{64}$Ni has been performed with particular emphasis placed on (1) the significance of the backward-angle data with respect to removal of potential ambiguities and (2) the extent to which $\alpha$ elastic scattering at this energy is sensitive to the interior detail of the potential. In the $^{58}$Ni case, six equivalent potentials are found to fit the diffraction scattering region ($\theta < 70°$), but only two of these simultaneously provide acceptable fits in the backward-angle region. It is shown that the detailed form of the real potential significantly affects the scattering only at distances beyond ~4 fm. The 60-MeV $\alpha$ probe is not sensitive to the detail of the total potential inside of ~3 fm in any way that affects the elastic cross section.

[NUCLEAR REACTIONS $^{58,60,62,64}$Ni($\alpha, \alpha$), $E = 60$ MeV; $^{60}$Ni($\alpha, \alpha$), $E = 75$ MeV; measured $\sigma(\theta)$; $\theta = 12$–$160°$, enriched targets. Optical-model analysis.]

## I. INTRODUCTION

In the past decade extensive measurements of the elastic scattering of $\alpha$ particles have been made for a wide range of target nuclei and bombarding energies. The observed cross sections have for the most part been analyzed in terms of a local complex optical potential with Woods-Saxon form factors for both real and imaginary parts [see Eqs. (1) and (2)]. Early analyses[1,2] were largely restricted to low-energy (~30-MeV) measurements within the forward hemisphere and the results indicated that the scattering data could be fitted equally well with a large number of potentials characterized by (1) discrete values of the real well depth $V_R$ in the range 20 to 400 MeV and (2) a relatively constant strong absorptive term. Igo[3] found that these equivalent potentials are essentially identical in the tail region (beyond 7–8 fm) and consequently deduced certain relationships satisfied by the potential parameters. Arguments were given by Drisko, Satchler, and Bassel[4] that these parameter relationships are roughly equivalent to requiring identical $S$-matrix reflection coefficients for angular momenta corresponding to the classical turning point of the motion; that is, the strong absorption radius (typically, 6–8 fm). It was shown that the scattering wave functions generated by the equivalent potentials do indeed predict essentially the same reflection from the nuclear surface, but differ in the number of nodes in the nuclear interior (for different values of the real well depth). Studies by Fernandez and Blair[5] and Jackson and Morgan[6] confirmed the sensitivity of the scattering to the tail region and determined that the only uniquely determined size parameter is, in fact, the strong absorption radius. Hence, the elastic scattering is apparently insensitive to the nuclear interior, presumably because of the strong absorption of $\alpha$ particles in the nuclear surface.

Recent elastic $\alpha$ scattering measurements have been performed at higher energies and, in some instances, over more extensive angular ranges. It is argued that if the $\alpha$-particle penetrability increases faster with energy than the $\alpha$-particle absorption (larger numbers of reaction channels are being opened), the scattering becomes more sensitive to the interior region of the potential and hence determines it more uniquely. For example, Hauser *et al.*,[7] in a study of $^{64}$Ni data within the forward hemisphere, found just two equivalent potentials while work by Smith and Goldberg[8] on 139-MeV $^{58}$Ni data, also measured within the forward hemisphere, resulted in a single potential. Similarly, Singh *et al.*,[9] in a study of $^{24}$Mg data extending out to 165°, found four equivalent potentials at

40 MeV, but only one at 80 MeV. Further, since backscattered $\alpha$ particles experience small angular momentum barriers and therefore deep penetration, backward angle measurements should also be sensitive to the interior region of the potential. Thus, for forward-angle 64-MeV $^{58}$Ni data, Weisser *et al.*[10] found six equivalent potentials while 60-MeV measurements by Singh *et al.*,[11] covering 10–165°, yielded a preliminary result of only two equivalent potentials.

The present work consists of an optical-model analysis of medium-energy $\alpha$ elastic scattering data measured over a wide angular range. The parameter space of the $\alpha$-nucleus optical potential is explored in detail with respect to both the ambiguities in the potential and the angular extent of the data. Various spatial regions of the extracted potentials are closely examined in an attempt to more uniquely specify the $\alpha$-nucleus interaction.

## II. EXPERIMENT

This experiment was performed using the sector-focusing cyclotron of the Naval Research Laboratory (NRL). The facility provided a momentum-analyzed 60-MeV $\alpha$ beam characterized by a beam profile diameter of 2.5 mm and a 200-keV energy spread [full width at half maximum (FWHM)], at 1 $\mu$A intensity. Reaction products were detected by an array of eight Si(Li) diodes, four mounted on each of two independently movable arms inside a 75-cm scattering chamber. Detector angular acceptance varied from $\frac{1}{2}°$ in the forward hemisphere to 1° in the backward hemisphere with corresponding solid angles between $\frac{1}{2}$ and 1 msr. The kinematic spreads for this scattering geometry, combined with the measured intrinsic detector resolution and the energy spreads in the incident beam as well as the target, yield over-all resolutions of 240 keV (FWHM) at 60° (for $\frac{1}{2}°$ angular acceptance) and 260 keV (FWHM) at 120° (for 1° angular acceptance), in agreement with observed values ranging from 250 to 300 keV. The excited states of the even Ni isotopes all lying above 1 MeV of excitation, this resolution was sufficient except at far forward angles where the elastic scattering is particularly strong and overlapped with contributions from light target contaminants.

The detectors were sufficient to stop 60-MeV $\alpha$ particles at full depletion depth (~2 mm). Pulse amplification, discrimination, and routing were done in a conventional fashion utilizing commercial modular electronics. Events were stored in the memory of the on-line EMR 6050 computer in 8×1024-channel configuration arrays as well as on magnetic tape (for off-line checking of the on-line analysis).

The nickel targets were isotopically enriched self-supporting foils on loan from Argonne National Laboratory.[12] Target thicknesses had been measured previously to within 10% by an $\alpha$-particle gauge. Table I lists the measured target thicknesses together with target enrichments, the bombarding energies, and angular ranges over which the differential cross sections were measured. Generally, the angular distributions were measured in 1–2° and 2–4° steps for the forward and backward regions, respectively. Relative errors in the differential cross sections are due primarily to counting statistics and geometrical errors between two or more detectors measuring the same datum point. In the forward hemisphere they are, at most, 5% while in the backward hemisphere they range from 5 to 50%. The absolute normalization error is due almost entirely to uncertainty in the target thickness (10%). Other contributions were estimated to be: (1) efficiency and calibration of the Faraday cup (5%); (2) solid-angle uncertainty (3%); (3) target nonuniformity and beam-drift effects (5%); and (4) dead-time losses ($\frac{1}{2}$%). Combining all of these effects gives an estimate of 13% for the total absolute error.

The measured cross sections are illustrated in Fig. 1. For purposes of comparing the gross features and for later discussions we divide the angular distributions into three parts: Region I (10 to 70°), region II (70 to 110°), and region III (110 to 165°). Region I exhibits the strong diffraction pattern characteristic[13] of forward $\alpha$ elastic scattering at medium energies. At first inspection the diffraction structure appears to be identical (apart from slight phase differences) for the four isotopes. However, the rate at which the diffraction maxima fall with angle increases with neutron number by about 25% from $^{58}$Ni to $^{64}$Ni. Even greater differences in average slope exist in region II where the slopes are decreasing with neutron number with, for example, the $^{58}$Ni cross section falling off more than twice as fast as that of $^{64}$Ni. Differences in structure are also apparent in region II: While the cross section for $^{58}$Ni is slightly oscillatory, that of $^{60}$Ni is more smooth

TABLE I. Target properties, bombarding energies, and experimental angular ranges.

| Target | Thickness (mg/cm$^2$) | Enrichment (%) | Bombarding energy (MeV) | Angular range (deg) |
|---|---|---|---|---|
| $^{58}$Ni | 1.10 | 99.69 | 59.6 | 12–160 |
| $^{60}$Ni | 0.931 | 99.10 | 58.1 | 15–157 |
| $^{62}$Ni | 0.963 | >95 | 58.2 | 15–159 |
| $^{64}$Ni | 0.864 | 94.82 | 58.3 | 12–160 |

and those of $^{62}$Ni and $^{64}$Ni are oscillating strongly. In region III the quality of the data is poor except for that of $^{58}$Ni. The prominent features of this region, however, are that the cross sections are roughly constant with angle (in contrast to regions I and II) and that their absolute values are decreasing strongly with increasing neutron number: The average values of the cross sections for $^{58}$Ni, $^{60}$Ni, $^{62}$Ni, and $^{64}$Ni in region III are in the ratio 1.99, 1.03, 0.64, 0.55. Thus, $^{64}$Ni has a backward-angle averaged cross section about one fourth that of $^{58}$Ni and one half that of $^{60}$Ni.

## III. OPTICAL-MODEL ANALYSIS

In a phenomenological optical-model analysis of $\alpha$ nucleus elastic scattering, the interaction between the $\alpha$ particle and the nucleus is characterized by a spherically symmetric local complex potential. In the present analysis the potential is of the usual form

$$V_{\rm opt}(r) = V_c(r) - V_R f(x_R) - i\left(W_V - 4W_D \frac{d}{dx_I}\right) f(x_I) \tag{1}$$

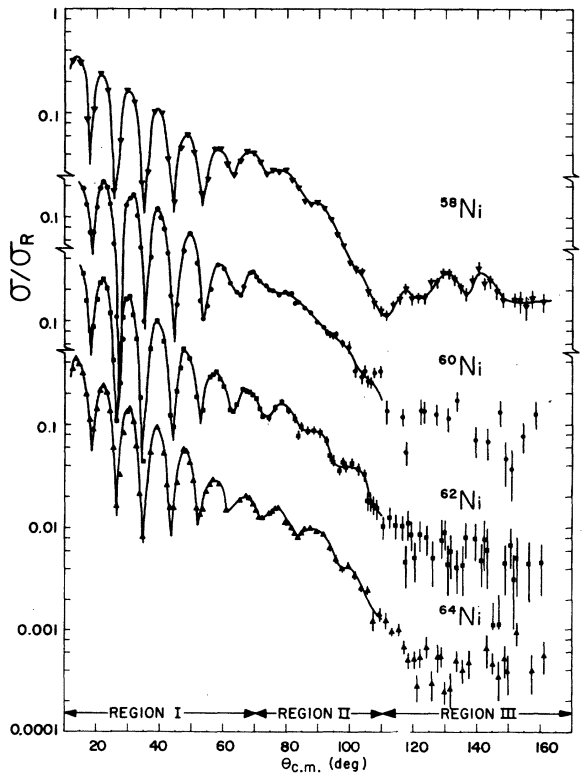


FIG. 1. Experimental differential cross sections for the elastic scattering of 60-MeV $\alpha$ particles by the even isotopes of nickel. The data is expressed as the ratio to Rutherford scattering (the curves drawn through the data points serve merely to guide the eye).

with Woods-Saxon form factors

$$f(x_j) = [1 + \exp(x_j)]^{-1}, \quad x_j = (r - r_j A^{1/3})/a_j \tag{2}$$

for both the real $(r_R, a_R)$ and imaginary $(r_I, a_I)$ potential wells. The first term represents the Coulomb interaction between a point $\alpha$ particle and the field of a uniformly charge sphere of radius $R_c = r_c A^{1/3}$. The remaining nuclear potential terms are the real central potential with volume form and the absorptive central potential with volume and/or surface (first derivative) forms. Retention of all terms in Eq. (1) allows for, at most, an eight-parameter model.

The optical-model search program OPTICAL[14] was used for all calculations, although consistency and accuracy checks were made with other existing optical-model codes.[15] The usual $\chi^2$ criterion was used as a quantitative measure of the goodness of fit. An automatic search routine adjusted the potential parameters to minimize the function $\chi^2{}_T$ given by

$$\chi^2{}_T = \sum_{i=1}^{N} \{[\sigma_t(\theta_i) - \sigma_e(\theta_i)]/\Delta\sigma_e(\theta_i)\}^2, \tag{3}$$

where $\sigma_t$ and $\sigma_e$ are the theoretical and experimental cross sections, respectively, at angle $\theta_i$, $\Delta\sigma_e$ is the relative error associated with $\sigma_e$, and $N$ is the number of data points. A related quantity used throughout this work is the $\chi^2$ per degree of freedom defined as $\chi^2{}_T/(N-M)$ where $M$ is the number of varied parameters. In all calculations of $\chi^2$, the actual errors $\Delta\sigma_e$ were used whenever they exceed the average (5%); otherwise, $\Delta\sigma_e/\sigma_e = 5\%$ was used.

### A. Procedures

Objective standards for an acceptable theoretical fit to the data were chosen as follows: (1) $\chi^2$ values changing by less than 0.001% on successive iterations terminated the search; (2) $\chi^2(\theta_i) \leq$ (constant), that is, the fit must be equivalently good over the entire angular range; (3) the best-fit parameter set must, within limits, be arrived at independent of the starting parameter set and the parameter search procedure; (4) an acceptable parameter set must be preceded by a final full search in which *all* model parameters are allowed to vary simultaneously.

Preliminary to the systematic analysis of the data, sensitivities of the model predictions to the following effects were investigated.

#### 1. *Absolute normalization errors in the data*

It is customary to treat this problem by performing normalization grids by which an optimum normalization constant is obtained within the limits of the estimated absolute error (13% for this work).

Normalization grids were performed in the following manner: A preliminary analysis of the $^{60}$Ni data, reported in Ref. 16, gave four best-fit parameter sets corresponding to real well depths $V_R$ of 120, 170, 220, and 288 MeV. By using these parameter sets as starting sets, four similar discrete potentials were found for each of the target nuclei. The normalization grid was then performed for the four potentials of each of the four nuclei and the final normalization constant was obtained by averaging the optimum values, giving 0.960, 1.024, 1.102, and 1.000 for $^{58}$Ni, $^{60}$Ni, $^{62}$Ni, and $^{64}$Ni, respectively. It is worthwhile to note that in any data renormalization the real potential parameters changed by at most 5% over a ±13% variation in normalization, while the imaginary potential parameters changed by as much as 30%.

*2. Size of the assumed nuclear charge distribution*

The radius parameter $r_c$ of the nuclear charge distribution was gridded over the range $1.10 \leq r_c \leq 1.40$ in order to optimize its value. It was found that small changes in $V_R, W_V$, and $a_I$ could always compensate for a change in $r_c$ such that the value of $\chi^2$ remained essentially constant. The optical-model fits are thus not very sensitive to the radius parameter $r_c$. Equivalently, $r_c$ is determined to within ~25%. For the remainder of this work its value has been arbitrarily set at 1.30 fm.

*3. Finite angular acceptances involved in the measurements*

Comparisons were made between optical-model calculations which minimized the $\chi^2$ function subject to averaging over the angular acceptance with those which did not. The differences between the predicted cross sections for the "smeared" and "non smeared" calculations never exceeded the minimum relative uncertainty of 5% over the entire angular range, and as a result the respective potential parameters differed by less than 1%. Hence, in the present case angle averaging of optical-model calculations is not required for determination of valid potentials.

*4. Uncertainties in the bombarding energies*

A series of calculations were performed to obtain a measure of the sensitivity of optical-model predictions to the magnitude of the bombarding energy. Fits to the $^{60}$Ni data were obtained for a sequence of energy values while holding all parameters fixed. Energy changes in excess of 400 keV (1 MeV) were required to produce a 50% (100%) increase in $\chi^2$. Parameter searches over a 1-MeV range in bombarding energy yielded parameters which changed smoothly with energy and differed, at the extremes, by less than 1%. The calibration of the beam momentum analysis magnet is believed accurate to within $\frac{1}{2}$% (±300 keV in this case) and the above results indicate that the data analysis is insensitive to an uncertainty in the beam energy of this magnitude.

### B. Results

*$^{58}$Ni.* The quality of the $^{58}$Ni data is superior to that of the other Ni isotopes studied. Hence this nucleus was singled out for a thorough analysis. In the first attempt to fit the $^{58}$Ni data, volume absorption and independent Woods-Saxon form factors were assumed for reasons of relatively high bombarding energy and extensive backward-angle data.[17] The starting values for $V_R, W_V$ were chosen as four times those of the nucleon-nucleus optical potential[18] at one fourth of the $\alpha$ bombarding energy. Two distinct potentials were immediately found; $(V_R, W_V) = (126$ MeV, 18 MeV) and (171 MeV, 22 MeV), both providing excellent fits in region I, but disagreeing somewhat in phase and magnitude with the oscillations observed in the data of regions II and III. Four additional potentials were found by holding the 18- and 22-MeV absorptive potentials fixed and searching on $(r_R, a_R)$ while gridding $V_R$ over the range 20–40 MeV. The absorptive parts of the four new potentials were then varied to achieve minimum $\chi^2$, after which full searches (i.e., on all parameters) were performed. Hence a total of six distinct potentials fit the data. Their most distinguishing feature is the large spacing of 45–90 MeV in the central well depth, $V_R$: 79.6, 126.7, 173.1, 228.2, 297.2, and 385.8 MeV. Other starting sets and search procedures led to the same potentials.[19] In particular, pairwise searching on any two of the three parameters characterizing either the real or absorptive well for any of the six potentials did not significantly alter their values.

The differential cross section predicted by each of the six potentials is compared to the experimental result in Fig. 2 and the six best-fit parameter sets are listed in Table II together with an indication of their quality of fit to the data. Specifically, the 79.6 and 126.7-MeV potentials fail to fit the data in region III (see Fig. 2) whereas the remaining potentials fit equivalently well. With the exceptions of the 297.2- and 385.8-MeV potentials, all potentials provide an excellent fit to the data within region I. However, none of the potentials are able to satisfactorily reproduce the angular structure of the data in region II, although they do predict the correct average slope and magnitude (except for the 79.6- and 385.8-MeV potentials). Over the entire angular range, only the 173.1- and 228.2-MeV potentials can be considered as equivalent best-fit potentials. It is immediately obvious that the inclu-

sion of extensive backward-angle data has reduced the number of acceptable potentials. In the $^{58}$Ni case six potentials exist. By comparing their predicted cross sections for the first 70° of the data four of the potentials are found to be equivalent. By comparing over the first 110° of the data only three are found equivalent and across the total angular range only two potentials give equivalently good over-all fits.

An attempt was made to improve the backward-angle fits by holding the real part of each potential fixed while adjusting the imaginary part. Adequate fits were obtained for a series of absorptive potentials with strengths ranging from 12 to 36 MeV, but no substantial improvement was found in the phase mismatch across regions II and III. On the contrary, it became clear that despite the inclusion of extensive backward-angle data, the absorptive potentials are not unique; that is, changes in one parameter can be compensated by changes in one or both of the remaining parameters, over limited ranges. Changing the absorptive interaction from volume to surface form [see Eq. (1)] yields minimum values of $\chi^2$ essentially equal to those obtained for volume absorption. Comparisons of the parameter sets reveal that for each of the six $^{58}$Ni potentials listed in Table II, volume and surface forms for the absorptive potential can be used interchangeably with only minor changes in the real potential parameters which are such that the rms radius of $V_R(r)$ remains constant to within 1%. Weisser *et al.* found similar results for 64-MeV $^{58}$Ni data extending just beyond region I.[10] Figure 3 compares the predicted cross sections and absorptive potentials for volume and surface absorption, in the case of the 170-MeV real potential for $^{58}$Ni. Clearly, the absorptive potentials are essentially identical in the surface region beyond 6.5 fm, but differ drastically in the interior region. The close agreement found between predicted differential and reaction cross sections for volume and surface absorption implies that 60-MeV $\alpha$-particle scattering is insensitive to the interior region of the absorptive potential. In part this may be due to the fact that the continuous ambiguity in the volume absorptive strength is large enough to span

TABLE II. Best-fit optical-model potentials for the scattering of 60-MeV $\alpha$ particles by the isotopes of nickel. All strengths in MeV and geometrical parameters in fm.

| Nucleus | $V_R$ | $r_R$ | $a_R$ | $R_{rms r}$ | $W_V$ | $r_I$ | $a_I$ | $R_{rms i}$ | $\sigma_R$ [a] | $J_R/A$ [b] | $\chi^2$ [c] | EPI, II, III [d] |
|---|---|---|---|---|---|---|---|---|---|---|---|---|
| $^{58}$Ni | 79.6 | 1.341 | 0.850 | 5.118 | 15.09 | 1.677 | 0.527 | 5.396 | 1652 | 1015 | 26.9 | I |
| | 126.7 | 1.295 | 0.781 | 4.837 | 18.04 | 1.642 | 0.506 | 5.235 | 1635 | 1428 | 13.6 | I, II |
| | 173.1 | 1.279 | 0.719 | 4.671 | 22.17 | 1.588 | 0.531 | 5.152 | 1634 | 1828 | 10.3 | I, II, III |
| | 228.2 | 1.254 | 0.692 | 4.554 | 25.23 | 1.577 | 0.515 | 5.102 | 1628 | 2260 | 13.0 | I, II, III |
| | 297.2 | 1.209 | 0.688 | 4.425 | 28.89 | 1.548 | 0.530 | 5.036 | 1636 | 2667 | 15.9 | II, III |
| | 385.8 | 1.149 | 0.701 | 4.323 | 31.34 | 1.541 | 0.525 | 5.016 | 1634 | 3052 | 17.7 | III |
| $^{60}$Ni | 59.2 | 1.468 | 0.685 | 5.131 | 19.02 | 1.626 | 0.507 | 5.279 | 1618 | 894 | 16.0 | I |
| | 116.0 | 1.335 | 0.695 | 4.805 | 20.64 | 1.568 | 0.564 | 5.175 | 1626 | 1356 | 10.2 | I, II |
| | 163.3 | 1.299 | 0.666 | 4.646 | 24.86 | 1.518 | 0.577 | 5.071 | 1624 | 1753 | 8.6 | I, II, III |
| | 215.2 | 1.272 | 0.643 | 4.533 | 29.04 | 1.484 | 0.580 | 4.984 | 1622 | 2159 | 9.3 | I, II, III |
| | 273.1 | 1.248 | 0.631 | 4.445 | 32.81 | 1.478 | 0.559 | 4.950 | 1613 | 2587 | 11.1 | I, II, III |
| | 341.8 | 1.216 | 0.629 | 4.368 | 36.12 | 1.479 | 0.537 | 4.909 | 1608 | 3016 | 12.6 | I, II, III |
| $^{62}$Ni | 48.8 | 1.505 | 0.660 | 5.224 | 23.44 | 1.542 | 0.605 | 5.236 | 1679 | 780 | 9.2 | I |
| | 110.1 | 1.355 | 0.674 | 4.865 | 24.92 | 1.504 | 0.637 | 5.151 | 1688 | 1325 | 8.2 | I, II |
| | 162.3 | 1.300 | 0.663 | 4.689 | 27.72 | 1.486 | 0.624 | 5.097 | 1686 | 1736 | 7.4 | I, II, III |
| | 217.2 | 1.263 | 0.649 | 4.566 | 32.88 | 1.447 | 0.631 | 5.014 | 1683 | 2136 | 8.3 | I, II, III |
| | 278.8 | 1.230 | 0.641 | 4.463 | 38.31 | 1.420 | 0.629 | 4.936 | 1680 | 2544 | 9.6 | I, II, III |
| | 369.1 | 1.157 | 0.672 | 4.336 | 39.56 | 1.454 | 0.581 | 4.954 | 1665 | 2900 | 10.0 | I, II, III |
| $^{64}$Ni | 38.8 | 1.538 | 0.633 | 5.292 | 27.61 | 1.408 | 0.765 | 5.209 | 1756 | 653 | 16.7 | I |
| | 110.8 | 1.335 | 0.682 | 4.863 | 25.09 | 1.487 | 0.639 | 5.253 | 1693 | 1282 | 13.7 | I, II |
| | 165.8 | 1.275 | 0.671 | 4.698 | 27.87 | 1.462 | 0.642 | 5.197 | 1683 | 1686 | 11.7 | I, II, III |
| | 224.1 | 1.235 | 0.659 | 4.591 | 30.57 | 1.441 | 0.644 | 5.113 | 1680 | 2068 | 11.6 | I, II, III |
| | 285.4 | 1.208 | 0.646 | 4.505 | 33.54 | 1.436 | 0.626 | 5.055 | 1675 | 2470 | 12.5 | I, II, III |
| | 357.2 | 1.173 | 0.647 | 4.361 | 37.00 | 1.438 | 0.598 | 4.980 | 1674 | 2868 | 14.1 | I, II, III |

[a] Theoretical reaction cross section in mb.

[b] Volume integral of the real part of the central potential divided by $A$ (MeV fm$^3$).

[c] $\chi^2$ per degree of freedom.

[d] Equivalent potentials for region I (10–70°) and/or region II (70–110°) and/or region III (110–165°). Note that the contribution of the $^{60}$Ni, $^{62}$Ni, and $^{64}$Ni region III data to $\chi^2$ is small (see Fig. 1, region III).

the variation of the corresponding surface absorptive strength between ~3 and ~6 fm. The conclusion here is that any smooth form for the absorptive potential is acceptable so long as it possesses the correct surface ($r > \sim 6$ fm) behavior.

The continuous parameter ambiguities within both real and imaginary potentials were independently studied: continuous real ambiguities (CRA) were determined with the absorptive potentials held fixed and continuous imaginary ambiguities (CIA) were investigated for fixed real potentials. The results of the parameter explorations are basically the same for all six potentials for each of the four nickel isotopes listed in Table II. Considering the CRA, as $V_R$ increases, $r_R$ decreases, and $a_R$ increases such that the rms radius, $R_{\mathrm{rms}r}$, of $V_R(r)$ remains relatively constant. The same behavior is found for the CIA. Figures 4 and 5 illustrate the CRA and CIA, respectively, for the case of $^{60}$Ni (which is entirely similar to that of $^{58}$Ni). Note that the variation of $\chi^2$ with $V_R$ is of a discrete nature whereas for $W_V$ the behavior is smooth. Table III contains the ranges of the parameters corresponding to $\chi^2$ values twice the $\chi^2$(min) values.[20] It is apparent that for any of the $^{58}$Ni potentials, changes in $V_R$ up to ~45% can be compensated by changes in $r_R$ and $a_R$ up to ~20 and ~30%, respectively, such that $R_{\mathrm{rms}r}$ changes by no more than ~5% while $\chi^2 \leq 2\chi^2$(min). For the CIA in the $^{58}$Ni potentials, the corresponding percentages are roughly similar. Thus, for a given potential family, the rms radii $R_{\mathrm{rms}r}$ and $R_{\mathrm{rms}i}$ are the only well-determined geometrical quantities.

The foregoing CRA studies were repeated with the region III data deleted and finally with both regions II and III data deleted. The objective was to see if increasingly restricted angular regions allowed the existence of even more potential families. However, the number of families remained constant. It would appear, therefore, that the total number of discrete families is determined by the forward-angle diffraction scattering alone (region I). Moreover, the potential parameters for each family are already largely determined by the diffraction region. In fact, by comparing best-fit potentials for region I data alone with those for all data, one finds that on the average, $W_V$, $a_R$, and $a_I$ values differ by only 8–10%; $V_R$, $r_R$, and $r_I$ values differ by only 2–4%; and the $R_{\mathrm{rms}r}$ and $R_{\mathrm{rms}i}$ values differ by only $\frac{1}{2}$ and 2%, respectively.

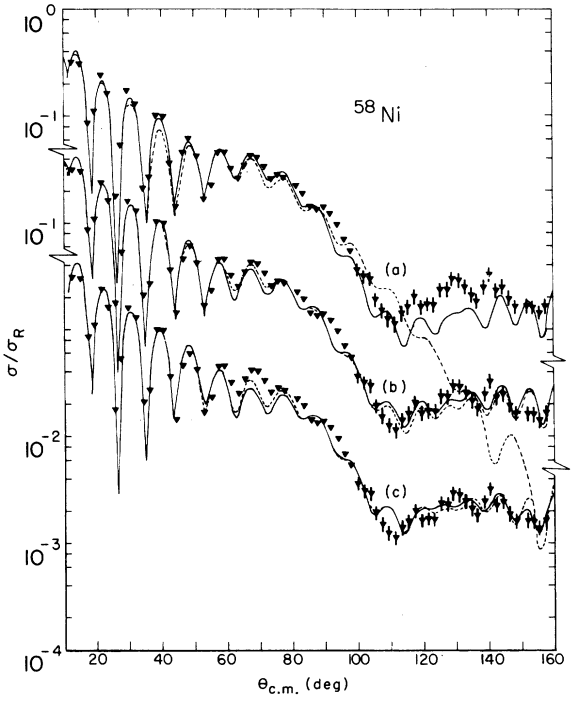


FIG. 2. Comparison of the best-fit optical-model predictions to the experimental data, for $^{58}$Ni: (a) 79.6 MeV (- - -) and 126.7 MeV (——); (b) 173.1 MeV (- - -) and 228.2 MeV (——); and (c) 297.2 MeV (- - -) and 385.8 MeV (——). The complete parameter sets are listed in Table II.

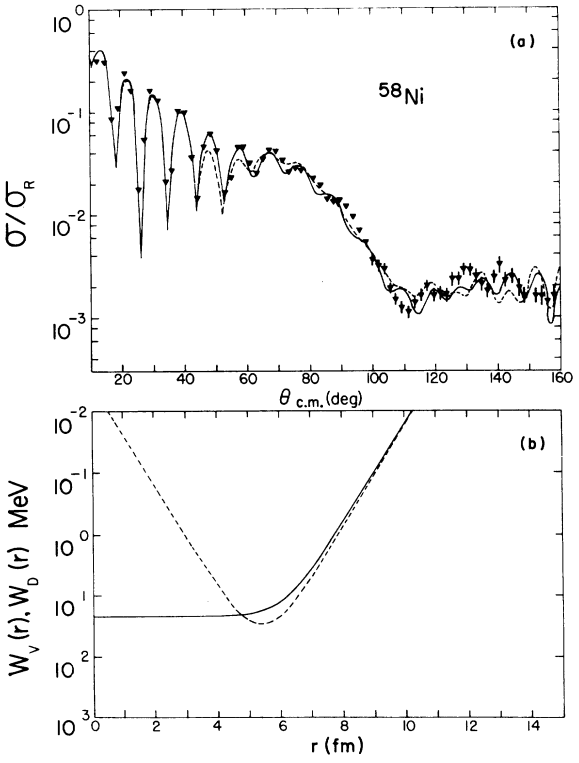


FIG. 3. Comparisons of $^{58}$Ni optical-model predictions (a) and absorptive potentials (b) for the cases of volume (——) and surface (- - -) absorptive form factors. The $V_R \sim 165$-MeV well is employed in both cases.

Thus, the rms radii are well determined by the diffraction scattering. Also, the backward-angle data is seen to be most sensitive to the absorptive strength and diffuseness parameters. In fact, it appears that the backward-angle sensitivity to these three parameters ($W_V$, $a_I$, $a_R$) is the mechanism that forces the acceptance range of the remaining three parameters ($V_R$, $r_R$, $r_I$) to be restricted to precisely those potentials of Table II designated as "equivalent" over the entire angular range.

*$^{60}Ni$, $^{62}Ni$, $^{64}Ni$.* Analysis of the $^{60}$Ni, $^{62}$Ni, and $^{64}$Ni data produced six potential families for each isotope, just as in the case of $^{58}$Ni. The best-fit parameters are listed in Table II. Calculated differential cross sections are illustrated in Fig. 6 for $^{62}$Ni as a representative case, together with the experimental data for comparison. Excellent fits to the region I (10-70°) data are achieved with all of the potentials. In region II (70–110°) the fits are generally good apart from a slight mismatch with the phase of the data. Despite the large experimental uncertainties in the region III data (beyond 110°),

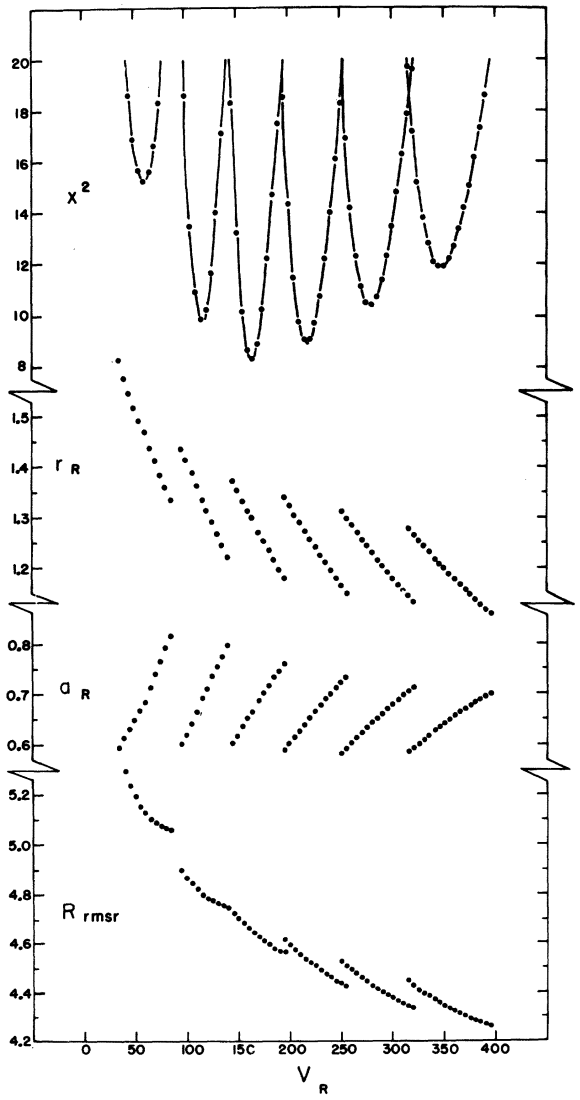


FIG. 4. Behavior of the continuous real ambiguities (CRA) in the six-family set of $^{60}$Ni. The absorptive potentials were held fixed (see Table II). The curve drawn through the $\chi^2$ vs $V_R$ points serves merely to guide the eye. Units are MeV and fm.

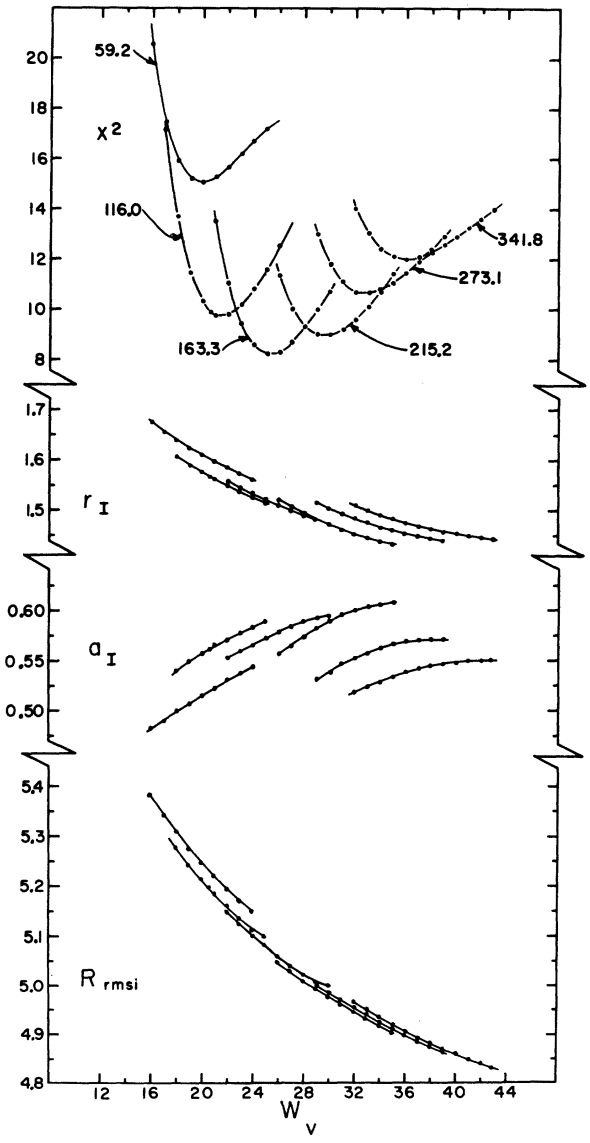


FIG. 5. Behavior of the continuous imaginary ambiguities (CIA) in the six-family set of $^{60}$Ni. The real potentials were held fixed (the $\chi^2$ vs $W_V$ curves are labeled with the appropriate $V_R$ values). The curves through the points serve merely to guide the eye. Units are MeV and fm.

the general trend is sufficiently clear to show that all but the ~50- and ~110-MeV wells provide equally good fits. Again, the inclusion of backward-angle data has reduced the number of acceptable potentials, although by fewer than the $^{58}$Ni case (presumably because of the better quality of the backward-angle $^{58}$Ni data—see Fig. 1). Similar conclusions hold for $^{60}$Ni and $^{64}$Ni.

There are obvious similarities among the parameter sets (Table II) obtained for the four isotopes:
(1) There exist six potentials per isotope. They are distinguished by the discrete spacing of the order of 50 MeV between values of $V_R$.
(2) The discrete values of $V_R$ are quite similar for the four isotopes and can be classified by the average values 55, 115, 165, 220, 280, and 365 MeV.
(3) The geometrical parameters of the Woods-Saxon form factor have the properties $r_R < r_I$ and $a_I < a_R$, in agreement with results of previous similar analyses.[6,10,13]
(4) For each isotope all potentials predict the same reaction cross section $\sigma_R$ to within 2%, and its value increases only slightly with increasing mass number.
(5) For each isotope, the rms potential radii, $R_{\mathrm{rms}r}$ and $R_{\mathrm{rms}i}$, are constant to within 9 and 4%, respectively. $R_{\mathrm{rms}r}$ shows a slight, although unsystematic, increase with mass number. No systematic trend is found for $R_{\mathrm{rms}i}$, which is probably connected with the observation that the parameters of the imag-

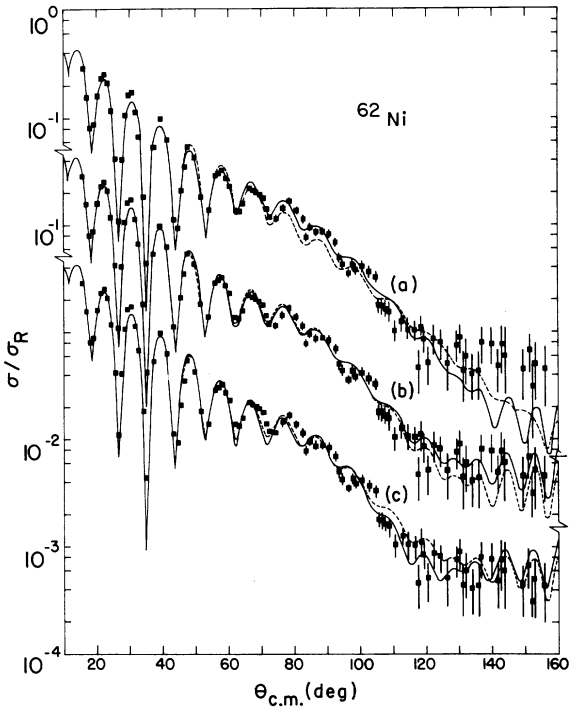


FIG. 6. Comparison of the best-fit optical-model predictions to the experimental data for $^{62}$Ni: (a) 48.8 MeV (- - -) and 110.1 MeV (——); (b) 162.3 MeV (- - -) and 217.2 MeV (——); and (c) 278.8 MeV (- - -) and 369.1 MeV (——). The complete parameter sets are listed in Table II.

TABLE III. Twice $\chi^2$(min) ranges of the continuous ambiguities in the optical-model potentials for the nickel isotopes. The twice $\chi^2$(min) range of each parameter is expressed as a percentage of the $\chi^2$(min) parameter value listed in Table II. The upper and lower parameter limits are approximately the Table II value plus or minus one half of the expressed percentage. The symbol > indicates that twice $\chi^2$(min) was never attained and that the tabulated percentage is a lower limit. Note that the shallowest and deepest wells of Table II have been deleted.

| Nucleus | $V_R$ | $\Delta V_R/V_R$ | $\Delta r_R/r_R$ | $\Delta a_R/a_r$ | $\frac{\Delta R_{\mathrm{rms}r}}{R_{\mathrm{rms}r}}$ | $W_V$ | $\Delta W_V/W_V$ | $\Delta r_I/r_I$ | $\Delta a_I/a_I$ | $\frac{\Delta R_{\mathrm{rms}i}}{R_{\mathrm{rms}i}}$ |
|---|---|---|---|---|---|---|---|---|---|---|
| $^{58}$Ni | 126.7 | 43 | 19 | 27 | 2 | 18.04 | 50 | 8 | 20 | 5 |
| | 173.1 | 40 | 21 | 29 | 4 | 22.17 | 45 | 10 | 30 | 4 |
| | 228.2 | 44 | 23 | 32 | 5 | 25.23 | 52 | 10 | 28 | 5 |
| | 297.2 | 52 | 29 | 37 | 6 | 28.89 | 66 | 11 | 25 | 6 |
| $^{60}$Ni | 116.0 | 34 | 14 | 25 | 2 | 20.64 | 126 | 15 | 16 | 10 |
| | 163.3 | 28 | 14 | 22 | 3 | 24.86 | 88 | 11 | 10 | 7 |
| | 215.2 | 26 | 14 | 21 | 4 | 29.04 | 148 | 15 | 12 | 10 |
| | 273.1 | 29 | 16 | 24 | 5 | 32.81 | 107 | 11 | 8 | 7 |
| $^{62}$Ni | 110.1 | 50 | 16 | 26 | 5 | 24.92 | >221 | >21 | >15 | >13 |
| | 162.3 | 37 | 16 | 24 | 4 | 27.72 | >206 | >18 | >11 | >12 |
| | 217.2 | 39 | 18 | 26 | 4 | 32.88 | >167 | >16 | >9 | >10 |
| | 278.8 | 41 | 18 | 24 | 6 | 38.31 | >146 | >14 | >9 | >11 |
| $^{64}$Ni | 110.8 | 68 | 24 | 42 | 5 | 25.09 | >187 | >18 | >11 | >12 |
| | 165.8 | 48 | 22 | 35 | 5 | 27.87 | 176 | 16 | 8 | 11 |
| | 224.1 | 51 | 25 | 37 | 6 | 30.57 | 92 | 33 | 73 | 3 |
| | 285.4 | 58 | 29 | 40 | 7 | 33.54 | 110 | 38 | 77 | 4 |

inary potential are quite sensitive to the absolute normalization of the data.

Obvious dissimilarities are noted among the measured differential cross sections of the four isotopes (see end of Sec. II). Most prominent among these is the pronounced decrease (by almost a factor of 4) in the angle-averaged cross section in region III with increasing mass number. One finds that the strength $W_V$ and diffuseness $a_I$ of the absorptive potential exhibit the greatest variation (by about 30 and 20%, respectively) between $^{58}$Ni and $^{64}$Ni (see Fig. 7). Even though these parameters are strongly influenced by the absolute normalization of the angular distributions as a whole, one can nevertheless attribute the large differences in the parameters $W_V$ and $a_I$ primarily to the large differences in the averaged backward-angle data.

Other results of the $^{60}$Ni, $^{62}$Ni, and $^{64}$Ni data analysis: Surface and volume absorptive potentials are substantially no different from one another and can be interchanged as long as the tail region ($r > 6$ fm) remains invariant. The CRA and CIA studies (Figs. 4 and 5 and Table III) indicate, again, that the rms radii are the only well determined shape parameters for a given family and that $\chi^2$ is much more selective in $V_R$ than in any other parameter. CRA studies performed on region I data only, regions I and II data, and finally on all of the data

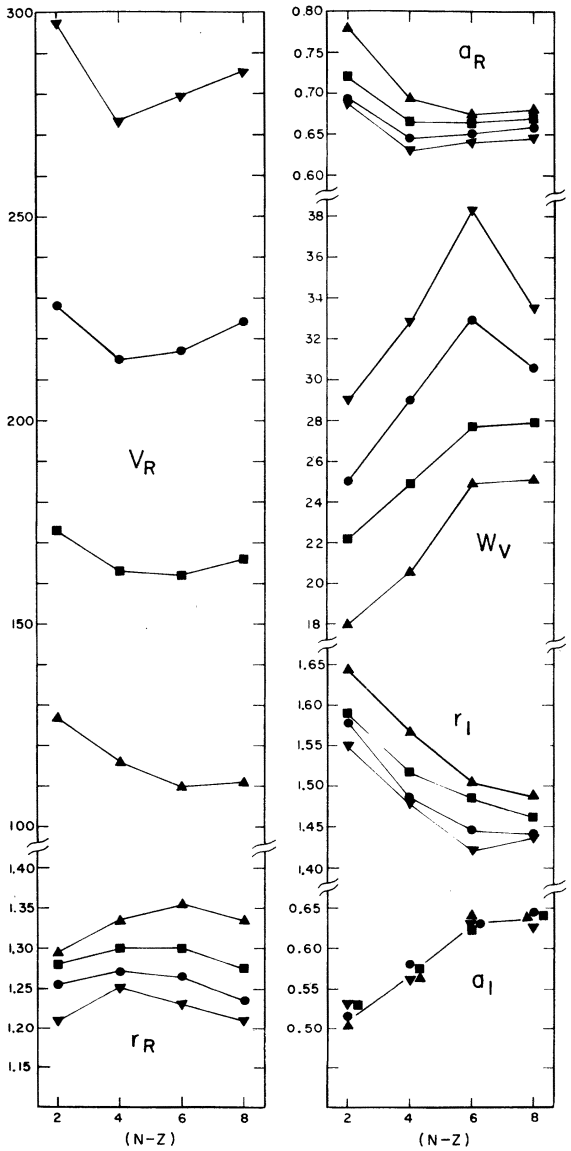


FIG. 7. Isotopic dependence of the optical-model parameters (Table II) found in the analysis of the scattering of 60-MeV $\alpha$ particles by the isotopes of nickel for the 115- (△), 165- (□), 220- (○), and 280-MeV (▽) wells (the shallowest and deepest wells have been deleted). Units are MeV and fm.

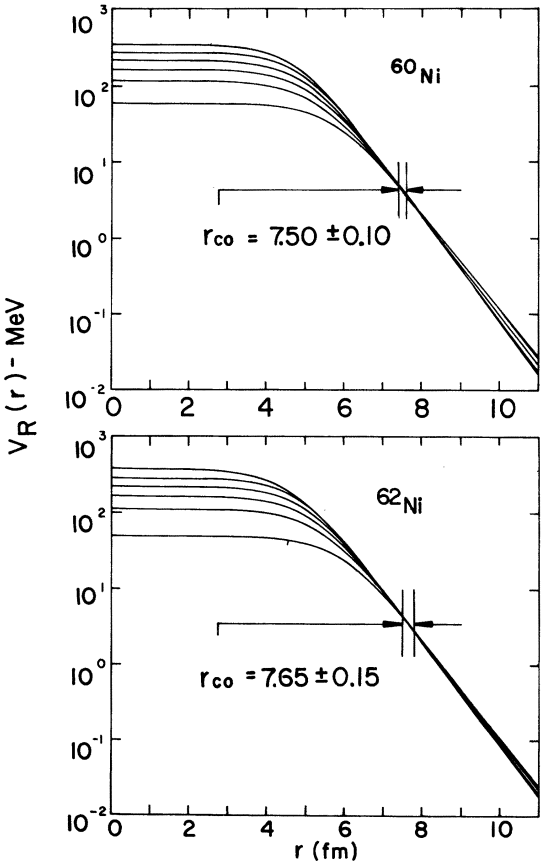


FIG. 8. Radial dependence of the real part of the optical potential for the six discrete potentials of $^{60}$Ni and $^{62}$Ni (see Table II). Log$V_R(r)$ is plotted to emphasize the similarities of the tails. The crossover radius $r_{CO}$ is the approximate coordinate at which the discrete potentials cross one another (see text).

gave the same number of discrete potentials, and ($W_V$, $a_I$, $a_R$) experience the greatest changes in comparing results of region I analyses to those obtained for the entire angular distribution. This again confirms our consistent observation that the backward-angle cross section depends strongly upon the absorptive strength and the diffuseness parameters.

## IV. DISCUSSION

The high quality of the over-all fits obtained with the present sets of equivalent potentials (see Table II) justifies their further study in the hope of extracting meaningful quantities which might provide clues for a more unique description of the scattering. Pursuant to this goal is the determination of what intrinsic properties and derived quantities are common to the sets of equivalent potentials and to what extent 60-MeV $\alpha$ particles probe the radial shape of the potential in various spatial regions. The answer to the last of these questions, moreover, is pertinent to the design of future experiments.

We first consider the extreme surface regions, or tails, of the equivalent potentials. Figure 8 illustrates logarithmic plots of the real parts of the $^{60}$Ni and $^{62}$Ni six-potential sets listed in Table II. The potentials are distinct inside of 5 fm (approximately the rms potential radius) and are essentially identical beyond 7 fm, in the tail of the potential. Inspection reveals that in almost all instances the potentials actually cross each other within a region less than 0.5 fm wide centered at almost 7.5 fm (designated as $r_{CO}$, the crossover radius). The same is true for the real potentials of $^{58}$Ni and $^{64}$Ni. Igo[3] in analysis of 18- to 48-MeV data has concluded that the strengths and geometries of the real and absorptive potentials can be varied, provided the tails do not change. For the real potential the Igo criterion is expressed by the invariance of the quantity $G_R$ given by

$$G_R = V_R^j \exp(r_R^j A^{1/3}/a_R^j), \tag{4}$$

where the index $j$ labels a particular discrete potential. The criterion is meaningful as long as the scattering is entirely a surface phenomenon. While this is not entirely true for the scattering of 60-MeV $\alpha$ particles, it was found that the parameter correlations within the CRA (see Fig. 4) are indeed consistent with relation (4).

In a study of the elements of the scattering matrix, $S_l = \exp(2i\delta_l) = \eta_l \exp(2i\delta_l^R)$, generated from optical potentials, Drisko, Satchler, and Bassel[4] have pointed out that the Igo criterion is roughly equivalent to requiring the reflection from the nuclear surface (as measured by the reflection coefficients Re$S_l$ and Im$S_l$) to be the same for those angular momenta corresponding to classical impact parameters in the tail region of the potential. The radius parameter associated with these angular momenta is the so-called strong absorption radius

TABLE IV. Strong absorption radii $r_{SA}$ and Igo criterion parameters $G_R$ defined by Eqs. (4) and (5) and calculated using the Table II potentials. The crossover radius $r_{CO}$ is the approximate coordinate at which the discrete potentials cross one another (Fig. 8). All strengths in MeV and geometrical parameters in fm.

| Nucleus | $V_R$ | $r_{CO}$ | $r_{SA}$ | $V_R(r_{CO})$ | $V_R(r_{SA})$ | $G_R \times 10^{-5}$ |
|---|---|---|---|---|---|---|
| $^{58}$Ni | 79.6 | 7.4 ±0.1 | 7.62 | 5.49 | 4.33 | 0.36 |
| | 126.7 | 7.4 ±0.1 | 7.60 | 5.68 | 4.49 | 0.78 |
| | 173.1 | 7.4 ±0.1 | 7.55 | 5.54 | 4.54 | 1.69 |
| | 228.2 | 7.4 ±0.1 | 7.54 | 5.60 | 4.61 | 2.54 |
| | 297.2 | 7.4 ±0.1 | 7.54 | 5.58 | 4.60 | 2.67 |
| | 385.8 | 7.4 ±0.1 | 7.54 | 5.64 | 4.41 | 2.20 |
| $^{60}$Ni | 59.2 | 7.5 ±0.1 | 7.49 | 4.24 | 4.32 | 2.61 |
| | 116.0 | 7.5 ±0.1 | 7.50 | 4.23 | 4.24 | 2.14 |
| | 163.3 | 7.5 ±0.1 | 7.49 | 4.22 | 4.29 | 3.38 |
| | 215.2 | 7.5 ±0.1 | 7.48 | 4.18 | 4.34 | 4.97 |
| | 273.1 | 7.5 ±0.1 | 7.48 | 4.26 | 4.42 | 6.29 |
| | 341.8 | 7.5 ±0.1 | 7.48 | 4.32 | 4.49 | 6.62 |
| $^{62}$Ni | 48.8 | 7.65±0.15 | 7.53 | 3.01 | 4.08 | 4.05 |
| | 110.1 | 7.65±0.15 | 7.56 | 3.09 | 4.06 | 3.14 |
| | 162.3 | 7.65±0.15 | 7.56 | 3.12 | 4.14 | 3.81 |
| | 217.2 | 7.65±0.15 | 7.55 | 3.08 | 4.15 | 4.01 |
| | 278.8 | 7.65±0.15 | 7.55 | 3.07 | 4.19 | 5.54 |
| | 369.1 | 7.65±0.15 | 7.56 | 3.26 | 4.29 | 3.36 |
| $^{64}$Ni | 38.8 | 7.65±0.1 | 7.56 | 3.32 | 3.76 | 6.46 |
| | 110.8 | 7.65±0.1 | 7.58 | 3.61 | 4.00 | 2.79 |
| | 165.8 | 7.65±0.1 | 7.58 | 3.62 | 4.03 | 3.32 |
| | 224.1 | 7.65±0.1 | 7.57 | 3.60 | 4.05 | 4.04 |
| | 285.4 | 7.65±0.1 | 7.56 | 3.58 | 4.11 | 5.06 |
| | 357.2 | 7.65±0.1 | 7.56 | 3.66 | 4.19 | 5.04 |

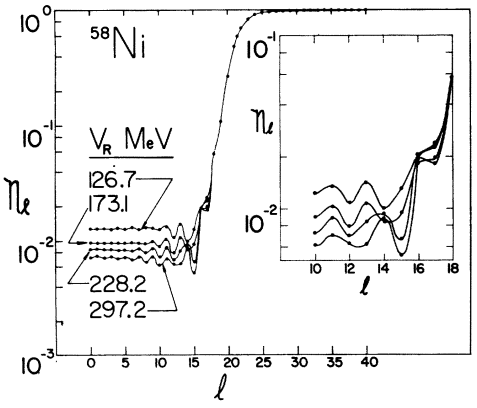


FIG. 9. Dependence of the amplitudes $\eta_l$ (of the elements of the scattering matrix $S_l$) upon the channel spin $l$ for scattering matrices generated from four discrete $^{58}$Ni potentials (Table II). The curves through the points serve merely to guide the eye.

$r_{SA}$, defined[5] as the classical turning point of motion for that critical angular momentum $l_0$ for which $\mathrm{Re}S_{l_0}=0.5$:

$$r_{SA}=(1/k)\{\nu+[\nu^2+l_0(l_0+1)]^{1/2}\}, \quad (5)$$

where $k$ is the wave number and $\nu$ is the Coulomb parameter. The strong absorption radii $r_{SA}$ and the Igo parameters $G_R$ have been calculated for all potential sets of Table II and are listed together with the crossover radii $r_{CO}$ in Table IV. The $r_{SA}$ values are constant to within $\frac{1}{2}\%$ for any of the six-potential sets and across the isotopic sequence they differ by less than 2%. Moreover, the strong absorption radius lies within the crossover region as illustrated, for example, in Fig. 8 (the corresponding critical angular momentum $l_0$ lies in the range $21<l_0<22$). Figure 9 illustrates $|S_l|=\eta_l$ as a function of $l$ for discrete $^{58}$Ni potentials. The curves indicate that the $\eta_l$ values are essentially identical for the significant $l$ values involved ($l=18$ to 25). Similarly, one finds essentially the same real phase shifts $\delta_l^R$ over the range of significant $l$ values. These observations confirm that the significant $S$ matrix elements are essentially equal for the set of discrete potentials; that is, they constitute a set of phase-shift equivalent potentials.

The Igo parameter $G_R$, on the other hand, fluctuates by factors as large as 6 for a six-potential set and across the isotopic sequence it changes by factors up to 18. Relation (4) shows that the Igo parameter is most sensitive to the diffuseness parameter $a_R$ which, in turn, is one of the parame-

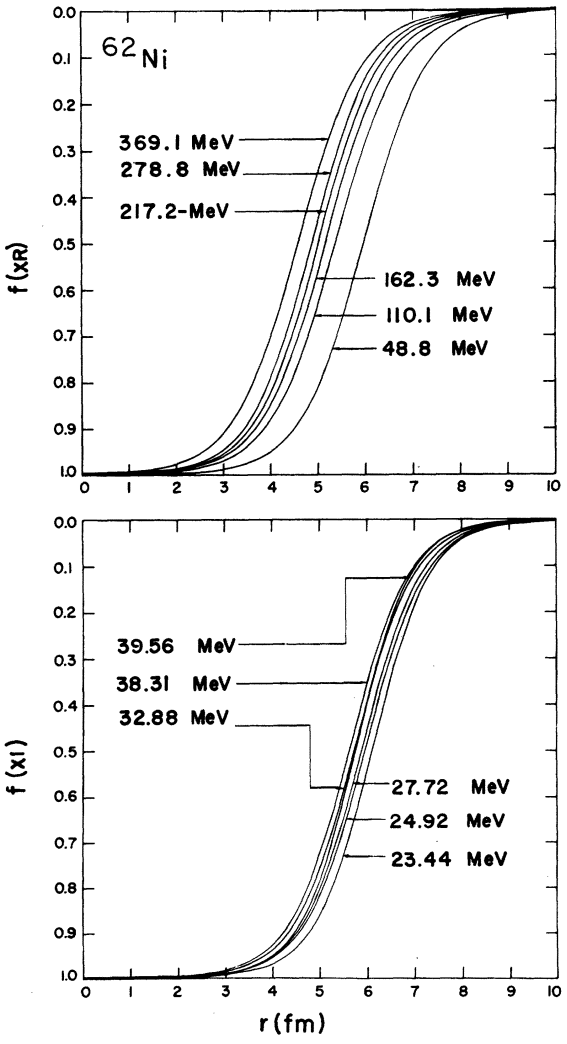


FIG. 10. Radial dependence of the real and imaginary form factors for the six discrete $^{62}$Ni potentials listed in Table II.

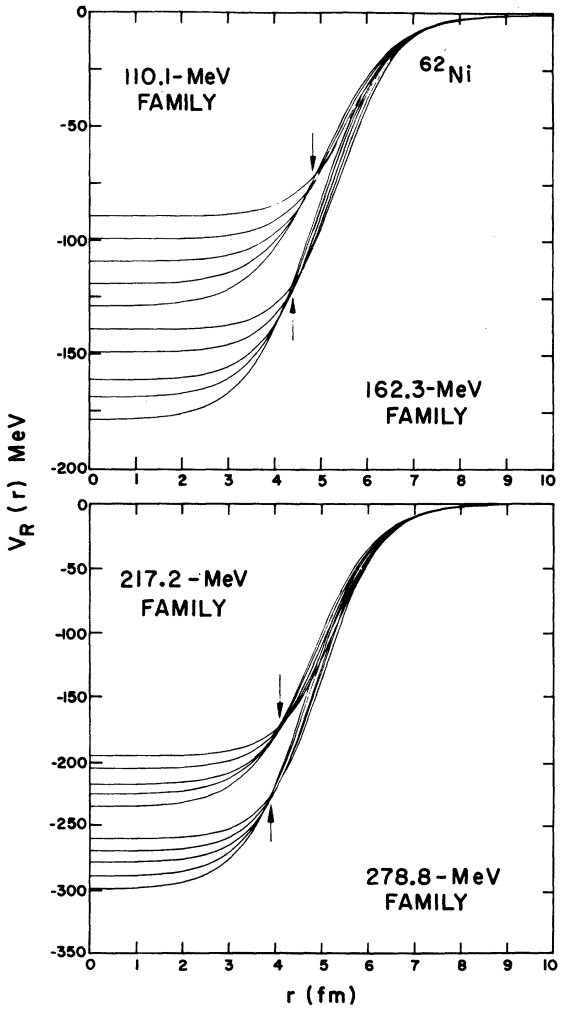


FIG. 11. Several members of the continuous family of real potentials for each of four discrete $^{62}$Ni potentials (Table II). An arrow indicates the radial coordinate at which the potentials converge and beyond which they remain very similar.

ters most sensitive to the backward-angle data (see Sec. III). Thus, one might expect to satisfy the Igo criterion for potentials which fit the forward-angle data alone. For $^{58}$Ni one finds that $G_R$ is indeed constant across the six-potential set to within 6% which represents a considerable improvement over the previous factor of 6, but is still poor in comparison to the $\frac{1}{2}$% variation in the strong absorption radius. Moreover, the strong absorption radii for the potential sets obtained from forward-angle data alone are identical to those for the potential sets which fit the whole angular distribution. Thus, while the Igo criterion is roughly satisfied for the diffraction scattering,[21] but fails upon the introduction of backward-angle data, the strong absorption radii are truly constant across the discrete ambiguities irrespective of the presence or absence of the backward-angle data.

We turn next to the investigation of the full surface region of the potentials. Figure 10 shows, for example, that the real and imaginary form factors for the $^{62}$Ni potentials have very similar slopes (similar diffuseness parameters) but different halfway radii such that the actual potentials (product of strength and form factor) for members of a given family are quite similar in radial shape beyond ~4 fm (Fig. 11). These similarities suggest that certain moments of the form factor may be conserved. In order to investigate this possibility the $k$th radial moments[22] were calculated for the real and imaginary parts of the Table II potentials (as well as for several members of their associated continuous families). For example, considering the real potential, the quantity $\langle r^2\rangle^{1/2}$ is just the rms potential radius $R_{\mathrm{rms}_r}$ which was found to be constant to within ~5% for the continuous family of any given well, and is determined to within 6% when averaged over the equivalent best-fit potentials (EP I, II, III of Table II). Similar results were obtained for the unnormalized $k=0$ moment of the real potential, which is just the volume integral $J_R$ given by

$$J_R = 4\pi \int_0^\infty r^2 U(r)\,dr. \tag{6}$$

Calculations showed that this quantity is essentially determined by the diffraction scattering, as is the rms radius, that it is constant to within ~7% for the continuous family of any given well, and that it is determined to within 10% when averaged over equivalent best-fit potentials.

Consideration of all values of $k$ through 8, however, yielded negative results in the sense that while conserved quantities could be found for a given family of a given isotope, the same quantities were not equally conserved in other families of the same isotope, nor were they equally conserved for corresponding families in two different isotopes. For example, looking at the $k$th root of the $k$th normalized radial moment $\langle r^k\rangle^{1/k}$, spanning the six families of real potentials for $^{60}$Ni, this quantity is essentially constant (to within <1%) for $k=6$, 4, 5, 5, 6, and 6, within the potential range about $V_R \sim 60$, 115, 165, 215, 275, and 340 MeV, respectively. Similar results are found for the normalized radial moments of the absorptive potentials. Repetition of these calculations for lower limits of ~4 fm on the moment integrals yielded no constant surface moments, contrary to expectations based on the similarities of the potentials in the surface region.

The unnormalized $k=2$ moment (dimensions MeV fm$^2$) is reminiscent of the well-known product relation $V_R r_R^k$ = constant, with $k \sim 2$. Accordingly, the exponent $k$ was calculated for a range of $(V_R, r_R)$ values corresponding to potentials satisfying $\chi^2 \leq 2\chi^2(\min)$ for the six potential families of each nickel isotope. Considering values of $V_R$ above 100 MeV, the mean values of $k$ are $1.85^{+0.35}_{-0.25}$, $1.92^{+0.48}_{-0.27}$, $2.23^{+0.82}_{-0.38}$, and $2.01^{+0.49}_{-0.36}$ for $^{58}$Ni, $^{60}$Ni, $^{62}$Ni, and $^{64}$Ni, respectively. These results are in general agreement with those obtained from low- and medium-energy nucleon scattering.[23] More recent analyses[24] of elastic proton scattering data have shown that the rms radius and volume integral of the real central potential are the most well determined quantities and the volume integral per target nucleon ($J_R/A$) is independent of target mass. In our case, inspection of Table II shows that $J_R/A$: (1) changes in discrete steps of ~400 MeV fm$^3$ across a six-potential set; (2) decreases slightly with increasing target mass for corresponding potentials; and (3) the slope of the mass dependence is the same for each potential family (with the exception of the ~55-MeV potential). It was noted earlier (Sec. III) that the rms radii are the most well determined geometrical quantities describing the nuclear surface.

We now consider the interior of the potential. Figure 11 illustrates several members of the continuous family of real potentials for each of four best-fit $^{62}$Ni potentials. An inspection of the graph shows that members of the 110-, 162-, 217-, and 269-MeV families are very similar for $r > 4.8$, 4.4, 4.1, and 3.9 fm, respectively (such remarks also apply to $^{58}$Ni, $^{60}$Ni, and $^{64}$Ni). The observed similarity in the radial dependence beyond ~4 fm indicates that the 60-MeV $\alpha$ probe determines the shape of the effective $\alpha$-nucleus potential for radii greater than ~4 fm. Conversely, one might suspect that the 60-MeV $\alpha$ probe may not be sensitive to the potential inside of ~4 fm. The sensitivity of the scattering to the inner potential region can be tested by significantly altering the potential within that

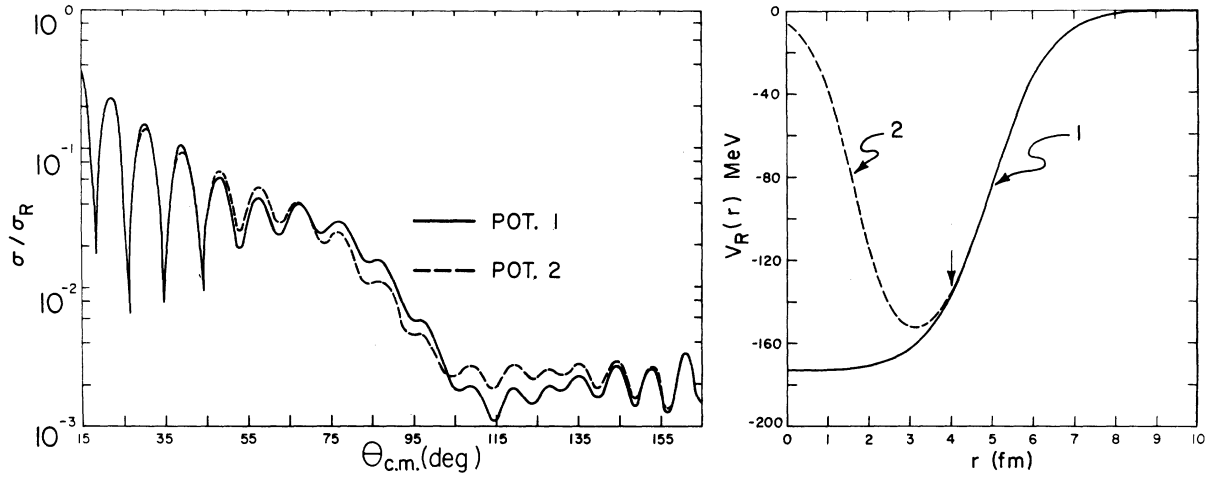


FIG. 12. Optical-model predictions for the illustrated real central potentials of $^{58}$Ni with volume absorptive form factors. The solid curve represents the best fit and the arrow indicates the coordinate of the 1% departure point from the best-fit real potential (Table II).

region without changing the potential in the surface region and comparing the predicted cross sections to the best-fit results. Such calculations were performed by introducing a soft core into the central potential which is now of the form

$$V_R(r) = V_R f(x_R) f(x_C), \tag{7}$$

where $f(x_R)$ is the usual Woods-Saxon form factor [Eq. (2)] and

$$f(x_C) = [F + \exp(x_C)] / [1 + \exp(x_C)], \tag{8}$$

with $x_C = (r - R_C/a_C)$, is the core form factor. For $F = 1$, Eq. (7) reduces to the standard Woods-Saxon potential. The soft-core calculations were performed with $F = 0$.

The 173-MeV $^{58}$Ni potential with volume absorption was chosen as a test case. The real central potential, for no core and a core beginning in the vicinity of 3 fm, together with the corresponding predicted cross sections, are illustrated in Fig. 12. The differences between the predicted cross sections are seen to occur primarily beyond the diffraction region which is to be expected, since low partial waves are associated with deep penetration and hence affect the backward-angle scattering. The result of a series of such calculations is summarized by Fig. 13, in which the solid curve is a plot of $\chi^2/\chi^2(\min)$ vs $r$, the radius at which the deviation from the Woods-Saxon form is 1%. The curve indicates that the departure of the cross section from the best fit, as the core moves outward in radius, becomes significant for $r \geq 4$ fm. Entirely similar results are obtained with the 228-MeV potential. Also, the equivalence of volume and surface absorption, noted earlier (Sec. III) in connection with a Woods-Saxon real form factor, is not affected by the introduction of a core, as indicated by the similarity of the solid (volume absorption) and dashed (surface absorption) curves in Fig. 13. The conclusion is that the 60-MeV $\alpha$ probe is not sensitive to the detail of the potential inside of 3 to 4 fm in any way that affects the differential cross section.

In this section we have attempted to find properties which are common to the six potentials making up the discrete ambiguity, as well as the continuous family of potentials associated with each discrete potential (continuous ambiguity). In the case of the *discrete* ambiguity the real potentials are essentially identical beyond ~7 fm (see Fig. 8) and consequently the *strong absorption radii* predicted by

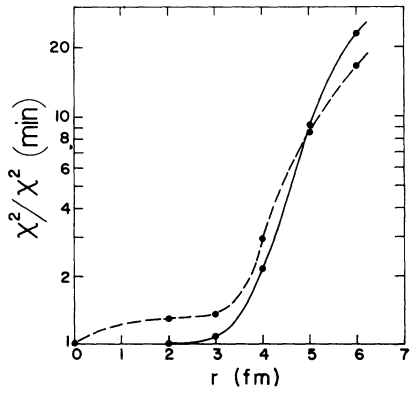


FIG. 13. Departure from best fit in $^{58}$Ni as a function of the position of a soft core introduced into the real central part of the best-fit potential [see Eq. (7)]. The coordinate $r$ is the 1% departure point from the Woods-Saxon potential (4 fm) for example, in Fig. 12. The solid and dashed curves represent the cases of volume and surface absorption, respectively.

all six potentials agree to within $\frac{1}{2}\%$. Secondly, the six potentials are *phase-shift equivalent* for $l \gtrsim 18$ (see Fig. 9). For $l \lesssim 18$, on the other hand, the amplitudes and phase shifts for different discrete potentials differ from one another by factors as large as 2 implying that, despite the weak amplitudes involved ($|S_l| \sim 10^{-2}$), it is these strongly absorbed low partial waves which are the signature of the discrete ambiguity. In the case of the *continuous* ambiguity the *rms radius* and the *volume integral* of the real potential are well determined quantities (to within ~6%) for a given family. Secondly, all potentials within the range of the continuous ambiguity are very similar beyond ~4 fm (see Fig. 11) and are, in fact, also *phase-shift equivalent* for $l \geq 18$. This is illustrated in Fig. 14 where the envelopes of all amplitudes and phases of the scattering matrix $S_l$ produced by extreme members of the continuous ambiguity range [$\chi^2 \sim 2\chi^2$(min)] are shown for two distinct families. Again, the very weak, but numerous low partial waves characterize the noticeable differences in the theoretical cross section even though the amplitudes $|S_l|$ differ by only ~10% over the range of the ambiguity.

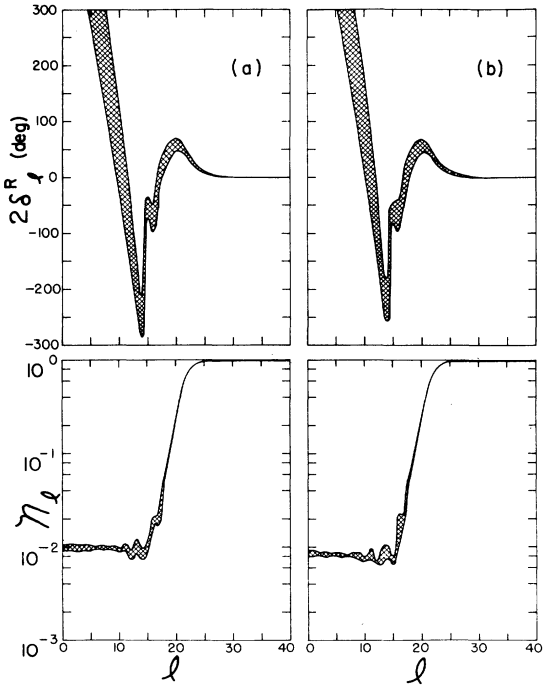


FIG. 14. The envelopes formed by all amplitudes and phase shifts of the $S_l$ produced by the extreme members of a twice $\chi^2$(min) family for the $^{58}$Ni cases of (a) the 173-MeV family and (b) the 228-MeV family.

## V. ADDITIONAL DATA

As soon as it became apparent in the present study of $\alpha$ scattering from Ni that one could not clearly distinguish between the four discrete, nearly phase-shift equivalent potentials obtained at 60-MeV bombarding energy, a program of additional measurements at somewhat higher energies was initiated at the NRL cyclotron. Due to intrinsic accelerator limitations and operational problems, the only experiment actually carried out was for $^{60}$Ni at 75.7-MeV bombarding energy. The resulting angular distribution is compared with the 60-MeV data in Fig. 15.

Although the energy of the additional measurements is only 25% higher, striking differences are observed. In contrast to the 60-MeV data, the 75-MeV cross section continues to decrease beyond 120° with a roughly exponential falloff (instead of leveling off) and a pronounced smooth hump has developed around 90° following the diffraction region. The characteristic features of the 75-MeV angular distribution are in fact represen-

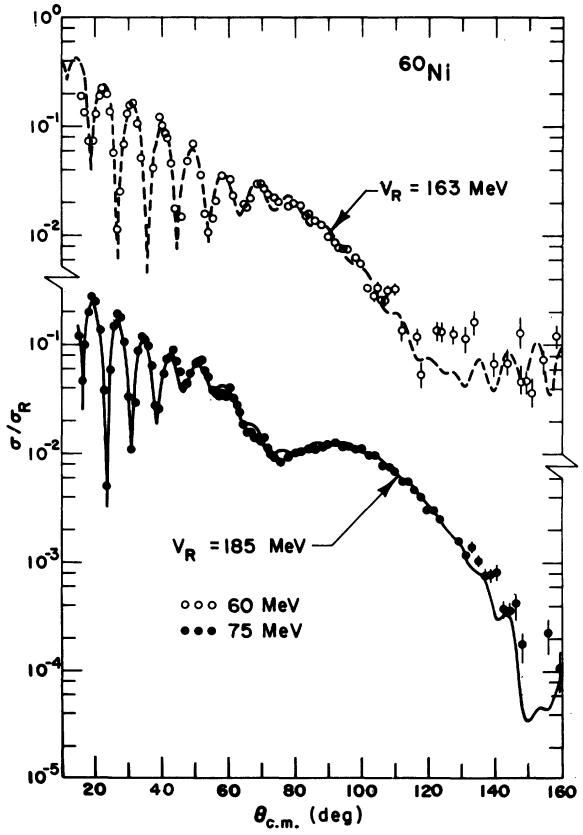


FIG. 15. $^{60}$Ni elastic differential cross sections (as ratio to Rutherford scattering) at 60 MeV (top) and 75 MeV (bottom). The curves are optical-model fits to the data obtained with similar potentials.

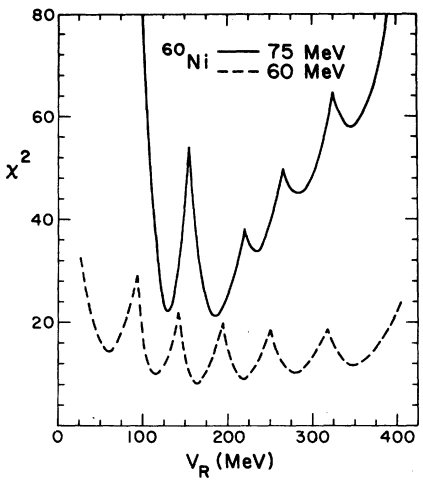


FIG. 16. Values of $\chi^2$ for fits to the $^{60}$Ni data obtained with different values of the real well depth $V_R$. The dashed curve is for 60-MeV, the solid curve for 75-MeV bombarding energy.

tative of higher-energy $\alpha$ -scattering such as, for example, $\alpha$+Ni scattering at 104 MeV[25] or $\alpha$+Pb scattering at 139 MeV.[26]

As is evident from Fig. 15, the features of the 75-MeV data are well reproduced by an optical potential which is essentially equivalent (within the continuous ambiguity) to that describing the 60-MeV results. The particular potential employed here for illustration belongs to the 170-MeV family of $V_R$ values. Although the best-fit parameter values differ somewhat at the two energies, both the rms radius and the volume integral of the real potential are nearly identical (within 1%).

An important difference in the optical-potential description at the two energies is observed, however, when the quality of fit is examined as a function of the parameter space. As can be seen from the $\chi^2$ versus $V_R$ curves of Fig. 16, at 75 MeV one can no longer fit the data with a very shallow potential ($V_R < 110$ MeV) or a very deep potential ($V_R > 210$ MeV). In effect, only two discrete, nearly equivalent potentials remain clearly acceptable at 75 MeV.

The evidence that one is beginning to remove the discrete potential ambiguity for $\alpha$+Ni scattering somewhat above 60 MeV (for data extending to 160°) supports the conclusions of a recent semiclassical description of the elastic scattering of complex projectiles by nuclei.[26,27] One of the criteria which was developed in that analysis for experimental data necessary to prevent the occurrence of multiple phase-shift equivalent potentials is a characteristic critical energy which must be exceeded. For $\alpha$+Ni, this critical energy turns out to be approximately 60 MeV. A second criterion is that the cross-section data extend well into the angular region of exponential falloff which is characteristic of energies in excess of the critical energy. At 75-MeV bombarding energy, these criteria are just beginning to be met.

Comparison of the 75-MeV $\alpha$+Ni case with the analysis[26] of $\alpha$+Pb data at 139 MeV (whose characteristic features are roughly similar) indicates that improved $\alpha$+Ni measurements at 75 MeV beyond 140° could serve to distinguish between the two acceptable potential families characterized by $V_R \sim 130$ MeV and $V_R \sim 185$ MeV. In both scattering cases, the characteristic large-angle minimum of the optical-model predictions occurs at a larger angle, and the large-angle falloff is less rapid, for the shallower potential; a clear distinction between the two discrete potentials thus seems possible on the basis of well-defined large-angle data.

## VI. CONCLUSIONS

The elastic scattering of 60-MeV $\alpha$ particles by the nickel isotopes was found to be well represented by a phenomenological optical potential, but the extraction of the potential from the data is not unique in the sense that the potential is determined only beyond some distance.

The problem of the nonuniqueness of the potential in this energy region is well known and is twofold: (1) One cannot clearly distinguish between a number of discrete nearly phase-shift equivalent potentials and (2) a given discrete potential itself is not unique, but is defined only within some range of continuous parameter ambiguities. Analysis of the data over restricted angular regions has shown that the diffraction scattering (region I) determines the extent of the discrete ambiguity. It has been further shown the the extent of the discrete ambiguity is diminished somewhat by the inclusion of backward-angle measurements. In fact, it was found that the absorptive strength and the diffuseness parameters are most sensitive to the backward-angle data. However, the fact that it has not been possible to resolve the discrete ambiguity for $\alpha$+Ni scattering at 60 MeV makes clear the need for even more extensive and accurate measurements, particularly at backward angles where the sensitivity to the low partial waves is greatest. As this analysis points out, it is indeed the collective effect of the large number of strongly absorbed, low partial waves which characterizes the discrete potential ambiguity. A survey of optical-model analyses[2,7-10,25-28] of $\alpha$+Ni scattering demonstrates that measurements at higher energy are needed to remove the discrete ambiguity. The present additional measurements at 75 MeV indicate that the minimum required energy (for data extending to 160°) is just

beyond 75 MeV.

Our study of the continuous ambiguity has shown that within a given family of potentials it is, again, the contribution of the low partial waves which distinguishes between family members. However, the low partial waves have little effect upon the rms radius and volume integral of the real potential; these remain constant to within about 5% for a given family and hence serve to characterize a given family far better than any particular potential parameter. Across the isotopic sequence studied, the rms radii show no systematic trend whereas the volume integrals systematically decrease slightly with increasing mass for corresponding potential families.

An investigation of the tails of the real and absorptive parts of the discrete potentials has shown that the total potential is uniquely determined at distances beyond ~6 fm. It has also been shown that the detailed form of the real potential significantly affects the scattering at 60 MeV only at distances beyond about 4 fm and that the 60-MeV $\alpha$ probe is not sensitive to the detail of the total $\alpha$+Ni potential inside of about 3 fm in any way that affects the elastic cross section.

## ACKNOWLEDGMENTS

We are grateful to Dr. R. G. Allas, Dr. J. J. Kolata, and Dr. D. A. Sink for their invaluable assistance in the data acquisition. We would also like to express our thanks to the entire operating staff of the cyclotron facility at the Naval Research Laboratory for their dedication and effort in providing the $\alpha$ beams under sometimes difficult conditions.

---

*Work supported in part by the National Science Foundation.

[1]G. R. Satchler, Nucl. Phys. 70, 177 (1965) and references contained therein.

[2]L. McFadden and G. R. Satchler, Nucl. Phys. 84, 177 (1966).

[3]G. Igo, Phys. Rev. Lett. 1, 72 (1958); Phys. Rev. 115, 1665 (1959).

[4]R. M. Drisko, G. R. Satchler, and R. H. Bassel, Phys. Lett. 5, 347 (1963).

[5]B. Fernandez and J. S. Blair, Phys. Rev. C 1, 523 (1970).

[6]D. F. Jackson and C. G. Morgan, Phys. Rev. 175, 1402 (1968).

[7]G. Hauser, R. Lohken, H. Rebel, G. Schatz, G. W. Schweimer, and J. Specht, Nucl. Phys. A128, 81 (1969).

[8]S. M. Smith and D. A. Goldberg, Bull Am. Phys. Soc. 17, 591 (1972).

[9]P. P. Singh, R. E. Malmin, M. High, and D. W. Devins, Phys. Rev. Lett. 23, 1124 (1969).

[10]D. C. Weisser, J. S. Lilley, R. K. Hobbie, and G. W. Greenlees, Phys. Rev. C 2, 544 (1970).

[11]P. P. Singh, W. T. Sloan, D. W. Devins, and P. Shapiro, Bull. Am. Phys. Soc. 16, 99 (1971).

[12]We wish to thank T. Braid and Argonne National Laboratory for the use of their enriched Ni targets.

[13]H. W. Broek, J. L. Yntema, B. Buck, and G. R. Satchler, Nucl. Phys. 64, 259 (1965); P. Darriulat, G. Igo, H. G. Pugh, J. M. Meriwether, and S. Yamabe, Phys. Rev. 134, B42 (1964).

[14]OPTICAL was written by G. T. Eckley, Department of Physics, Indiana University, 1968 (unpublished).

[15]Other optical-model codes used were SNOOPY3 by P. Schwandt, Department of Physics, Indiana University, 1972 (unpublished), and RAROMP by G. J. Pyle, University of Minnesota, Williams Laboratory Report No. COO-1265-64, 1968 (unpublished).

[16]W. T. Sloan, P. Schwandt, D. G. Madland, P. Shapiro, and P. P. Singh, Bull. Am. Phys. Soc. 16, 601 (1971).

[17]Four-parameter model studies, in which real and imaginary form factors were constrained to be identical, yielded unrealistic backward-angle fits.

[18]F. D. Becchetti, Jr., and G. W. Greenlees, Phys. Rev. 182, 1190 (1969).

[19]A Coulomb matching radius of 15 fm, an integral step size of 0.1 fm, and 40 partial waves were found sufficient for 60-MeV $\alpha$ particles on mass-60 targets.

[20]The results of the CRA and CIA studies for the deepest and shallowest potentials of Table II have not been summarized in Table III. The results are, however, illustrated in Figs. 4 and 5 (the $^{60}$Ni case) for comparisons with the other four potentials.

[21]Weisser *et al.* (Ref. 10) in an analysis of 64-MeV $^{58}$Ni data extending to 80°, find $G_R$ values constant to within 15% for their six-potential set.

[22]The $k$th radial moment of the potential $U(r)$ is defined as

$$\langle r^k \rangle = \frac{\int_0^\infty r^k U(r) d^3 r}{\int_0^\infty U(r) d^3 r} .$$

If the denominator is removed, the unnormalized $k$th radial moment of the potential is obtained. If the lower limits of the integrals are made finite, the corresponding surface moments are calculated.

[23]P. E. Hodgson, *The Optical Model of Elastic Scattering* (Clarendon Press, London, 1963), Chap. 5.

[24]H. S. Liers, R. N. Boyd, C. H. Poppe, J. A. Sievers, and D. L. Watson, Phys. Rev. C 2, 1399 (1970); W. Makofske, G. W. Greenlees, H. S. Liers, and G. J. Pyle, Phys. Rev. C 5, 750 (1972).

[25]H. Rebel, R. Loehken, G. W. Schweimer, G. Schatz, and G. Howser, Z. Phys. 256, 258 (1972).

[26]D. A. Goldberg, S. M. Smith, H. G. Pugh, P. G. Roos, and N. S. Wall, Phys. Rev. C 7, 1938 (1973).

[27]D. A. Goldberg and S. M. Smith, University of Maryland Technical Report No. 72-119 (unpublished).

[28]J. N. Simonov, K. O. Terenetskii, and V. V. Tokarerskii, Yad. Fiz. 14, 104 (1971) [transl.: Sov. J. Nucl. Phys. 14, 59 (1972)].